Journal of Marine Research, 74, 133–159, 2016

Carbon cycling in Santa Barbara Basin sediments: A modeling study

by David J. Burdige[1,2], Tomoko Komada[3], Cédric Magen[4,5], and Jeffrey P. Chanton[5]

ABSTRACT

The primary input of organic matter to almost all marine sediments comes from deposition at the sediment surface. However, in many continental margin settings, reduced carbon can also be added to sediments from below—for example, from "deep" geologic hydrocarbon reservoirs derived from ancient source rocks or from the decomposition of deeply buried gas hydrate deposits. To examine the impact of these two differing reduced carbon inputs on sediment biogeochemistry, a modified reaction-transport model for anoxic marine sediments is described here and applied to data from sediment cores in Santa Barbara Basin to a depth of 4.6 m. Excellent model fits yield results consistent with previous studies of Santa Barbara Basin and other continental margin sediments. These results indicate that authigenic carbonate precipitation in these sediments is not centered around the sulfate-methane transition zone (SMTZ), as is seen in many other sedimentary environments but occurs at shallower depths in the sediments and over a relatively broad depth range. Sulfate profiles are linear between the surface sediments (upper ∼20 cm) and the top of the SMTZ (∼105 cm) giving the appearance of refractory particulate organic carbon (POC) burial and conservative sulfate behavior in this intermediate region. However, model results show that linear profiles may also occur when high rates of sulfate reduction occur near the sediment surface (as organoclastic sulfate reduction [oSR]) and in the SMTZ (largely as anaerobic oxidation of methane) with low, but nonzero, rates of oSR in-between. At the same time, linearity in the sulfate profile may also be related to downward pore-water advection by compaction and sedimentation plus a decrease with depth in sulfate diffusivity because of decreasing porosity. These model-determined rates of oSR and methanogenesis also result in a rate of POC loss that declines near-continuously in a logarithmic fashion over the entire sediment column studied. The results presented further here indicate the importance of a deep methane flux from below on sediment biogeochemistry in the shallower sediments, although the exact source of this methane flux is difficult to ascertain with the existing data.

Keywords: Methane, sulfate reduction, anoxic sediments, anaerobic oxidation of methane

1. Department of Ocean, Earth and Atmospheric Sciences, Old Dominion University, Norfolk, VA 23529.
2. Corresponding author: ***e-mail: dburdige@odu.edu***
3. Romberg Tiburon Center, San Francisco State University, 3150 Paradise Drive, Tiburon CA 94920.
4. Chesapeake Biological Laboratory, University of Maryland, 146 Williams Street, P.O. Box 38, Solomons, MD 20688.
5. Department of Earth, Ocean and Atmospheric Science, Florida State University, P.O. Box 3064520, Tallahassee, FL 32306-4520.

Table 1. Key biogeochemical processes occurring in Santa Barbara Basin sediments.

Biogeochemical process	Reaction
Organoclastic sulfate reduction (oSR)	$POC + L_2\ SO_4^{2-} \rightarrow HCO_3^- + L_2\ H_2S$
Anaerobic oxidation of methane (AOM)	$CH_4 + SO_4^{2-} \rightarrow HCO_3^- + HS^- + H_2O$
Methanogenesis (methane production or MP)	$POC \rightarrow L_3\ CO_2 + L_2\ CH_4$
Authigenic carbonate precipitation (ACP)	$Ca^{2+} + CO_3^{2-} \rightarrow CaCO_3$

L_2 is either the ratio of the moles of sulfate reduced per mole of particulate organic carbon (POC) oxidized during oSR or the moles of methane produced per mole of POC oxidized during MP. L_3 is the ratio of the moles of dissolved inorganic carbon produced per mole of POC consumed during MP. For POC whose carbon oxidation state is ox, $L_2 = (4 - ox)/8$ and $L_3 = (4 + ox)/8$ (Burdige 2006; Burdige and Komada 2011). For example, if $ox = 0$ (i.e., POC is CH_2O), then $L_2 = L_3 = 1/2$. In this study, we assume $ox = -0.7$ (Burdige 2006), giving $L_2 = 0.59$ and $L_3 = 0.41$. Also note that $r_{C:S}$ equals $1/L_2$.

1. Introduction

The primary input of organic matter to all marine sediments comes from deposition at the sediment surface, or, when sediments receive enough light, production by benthic algae. However, reduced carbon can also be added to sediments from below—from "deep" geologic hydrocarbon reservoirs derived from ancient source rocks or from the decomposition of deeply buried gas hydrate deposits. Such gas hydrate deposits are common in many continental margin settings (e.g., Bohrmann and Torres 2006), including, for example, Santa Monica Basin (SMB) (Hein et al. 2006; Normark, Piper, and Sliter 2006; Paull et al. 2008) and Santa Barbara Basin (SBB) (Hill, Kennett, and Spero 2004; Leifer et al. 2006). From the standpoint of sediment biogeochemistry, however, it is important to note that such a deep methane flux is uncoupled from contemporaneous surface organic carbon fluxes and in situ methanogenesis derived from surface carbon inputs and likely results in distinct geochemical signatures in the sediment pore waters (Burdige and Komada 2011).

In sediments with such deep methane sources, or those in which there is in situ methanogenesis, once sulfate concentrations approach zero, one observes a sulfate-methane transition zone (SMTZ), which represents a locus of anaerobic oxidation of methane (AOM; see Tables 1 and 2). Here, the downward flux of sulfate meets the upward flux of methane, and because of the associated production of bicarbonate by AOM, this interface is frequently a major site for authigenic carbonate precipitation (ACP; e.g., Reeburgh 2007). Microbial processes appear to be stimulated at the SMTZ (e.g., Parkes et al. 2005; Inagaki et al. 2006; Harrison et al. 2009), although the details of how this occurs are not well understood (also see Berelson et al. 2005).

In past work, we examined the impact of such deep methane fluxes on pore-water profiles in SMB sediments (Burdige and Komada 2011) and the relationship between these deep methane fluxes and upward fluxes of other remineralization end products such as dissolved inorganic carbon (DIC) or ammonium (Burdige and Komada 2013). Here we extend our examination of these processes using an expanded version of the reaction-transport (RT)

Table 2. Model variables and parameters.

Term	Description	Value	Units
A	Concentration of dissolved ammonium [a]		mM
$ACP(z)$	The depth distribution of the rate of authigenic carbonate precipitation (ACP) (equation 10)		mM y^{-1}
Ca	Concentration of dissolved Ca^{2+} [a]		mM
D_x^s	Bulk sediment diffusion coefficient for species x corrected for tortuosity, determined using the modified Weissberg equation (Boudreau 1997): $$D_x^s = \frac{D_x^o}{1 - 2\ln\varphi}$$ [b]		cm^2 y^{-1}
D_x^o	Seawater, free solution diffusion coefficient for species x [c]		cm^2 y^{-1}
DIC	Concentration of DIC [a]		mM
$\Im$	A parameter that converts carbon concentrations in units of wt% C to mM and is given by $$\Im = 10^4 \cdot (\rho_{ds}/12)\frac{1-\varphi}{\varphi}$$ [b]		mM wt% C^{-1}
f_S	A function that inhibits the occurrence of methanogenesis when sulfate concentrations are above some threshold value (see Appendix) [d]		
F_{sed}	Mass accumulation rate to Santa Barbara Basin sediments [e]	0.1	g cm^{-2} y^{-1}
G_i	Concentration of metabolizable particulate organic carbon (POC) in fraction i ($i = 1 - 3$) [a]		wt% C
G_i^o	Concentration of metabolizable POC in fraction i at the sediment surface ($i = 1 - 3$)[d]		wt% C
J_{lbx}	The basal diffusive flux of solute x [d]		mmol m^{-2} d^{-1}
k_i	First-order rate constant for G_i degradation ($i = 1 - 3$) [d]		y^{-1}
k_{aom}	Second-order rate constant for anaerobic oxidation of methane (AOM) [d]		mM^{-1} y^{-1}
K_a	AOM half-saturation constant (Dale et al. 2008)	1	mM
K_{in}	A parameter that controls the steepness of the transition of f_S from 0 to 1 around the sulfate concentration S^* (equation A1) [d]		mM
K_m	Half-saturation constant for organoclastic sulfate reduction (oSR) (Burdige and Komada 2011)	0.5	mM
K_n	Dimensionless reversible ammonium adsorption coefficient (Mackin and Aller 1984)	1.3	
L_2	The ratio of sulfate reduced per mole of POC oxidized during oSR and moles of methane produced per mole of POC oxidized during methanogenesis [f]	0.59	

(Continued)

Table 2. (Continued)

Term	Description	Value	Units
L_3	The ratio of the moles of DIC produced per mole of POC consumed during methanogenesis [f]	0.41	
M	Concentration of pore-water methane [a]		mM
$R_{\max}$	The maximum rate of ACP [g]		mM y^{-1}
r_{NCi}	The nitrogen-to-carbon atomic ratio in the ith fraction of organic matter undergoing remineralization [d]		
s_{cp}	The parameter defining the width of the Gaussian function for the depth distribution of ACP (equation 10) [g]		cm
S	Concentration of pore-water sulfate [a]		mM
$S*$	The sulfate concentration around which f_S transitions from 0 to 1 (equation A1) [d]		mM
SMTZ	Sulfate-methane transition zone		
z	Sediment depth (positive downward) [b]		cm
z_{cp}	The sediment depth of maximum ACP (equation 8) [g]		cm
υ	Pore-water advection [b]		cm y^{-1}
φ	Sediment porosity (see equation 1) [b]		
φ_o	Porosity at the sediment-water interface (see equation 1)	0.99	
φ_∞	Porosity at great depth in the sediments (see equation 1)	0.78	
ρ_{ds}	Dry sediment density	2.65	g cm^{-3}
ω	Sediment accumulation (burial) rate [b]		cm y^{-1}

[a] Dependent variable.
[b] For these variables, a single value is not used because the variable changes either directly or indirectly with depth. In the latter case, for example, because porosity (φ) varies with sediment depth, so does $\Im$ and the various D_s values (because they are all a function of φ).
[c] See Table 3.
[d] Adjustable fitting parameter in the organic matter/methane/sulfate/ammonium model.
[e] Based on a range of values reported in the literature determined with either sediment core or sediment trap results (Bruland et al. 1981; Schimmelmann, Lange, and Berger 1990; Reimers et al. 1996; Thunell 1998).
[f] See Table 1.
[g] Adjustable fitting parameter in the Ca^{2+} model equation.

model that we used in these previous studies and apply this model to pore-water profiles of sulfate, methane, ammonium, and DIC from a series of multicores and gravity cores collected in SBB (Komada et al. 2016). Because these cores span a sediment depth of ~4.5 m and represent >2,000 years of sediment deposition, we are able to quantitatively examine diagenetic processes in nearshore sediments on timescales that are longer than those generally examined in previous studies of these same sediments or other California Borderland basin sediments (e.g., Sholkovitz 1973; Jahnke 1990; Reimers et al. 1996; Prokopenko et al. 2006). The development here of this model is also part of our ongoing work linking the results of RT models of inorganic pore-water constituents to models of dissolved organic matter cycling in sediments (e.g., Komada et al. 2013).

2. Field site and methods

The pore-water data examined here were obtained from sediment cores collected in the SBB, one of the inner basins of the California Borderland (Emery 1960). Cores were collected from the center of the basin (34.223° N, 119.983° W; 590 m water depth) using a gravity corer and a multicorer onboard R/V *Robert Gordon Sproul* in August 2012, and R/V *New Horizon* in August 2013. Details about coring and pore-water collection and processing can be found in Komada et al. (2016). The water column below the SBB sill depth (475 m) is low in dissolved O_2 (Sholkovitz 1973), and bottom-water dissolved O_2 concentration at the time of our sampling was $\sim$2 μmol kg^{-1} (Komada et al. 2016). As a result, the sediments in the central part of the basin are anoxic and varved (Soutar and Crill 1977; Reimers et al. 1990).

3. Field data

a. Data description

Because all of the data used here have been described previously (Komada et al. 2016), only a very brief description of the results is presented. The sulfate, methane, and DIC pore-water profiles indicate that sulfate reduction occurs in the upper $\sim$125 cm of SBB sediments and methanogenesis occurs below this depth (Fig. 1). From these observations, we defined the 125 $\pm$ 20 cm depth interval as the SMTZ (Komada et al. 2016). Both the DIC and SO_4^{2-} profiles show curvature in the uppermost $\sim$30 cm and in the SMTZ but were approximately linear in-between. The DIC profile also shows a distinct slope break across the SMTZ, which is likely because of a combination of an increased rate of DIC production in the SMTZ via AOM along with a decreased rate of DIC production (per mole of particulate organic carbon [POC] oxidized) in the deeper methanogenic sediments (Table 1). Total alkalinity pore-water profiles (data not shown here) also show a similar slope break across the SMTZ, likely for these same reasons. Concentrations of ammonium (Fig. 1) increased steadily with sediment depth, although unlike DIC, did not show a clear slope break across the SMTZ.

Methane concentrations are $<$1 mM above the SMTZ but increase sharply through this zone. Curvature in the methane profile through the SMTZ is consistent with the occurrence here of AOM (Reeburgh 2007). Pore-water Ca^{2+} concentrations decrease in an exponential-like fashion from the bottom-water value ($\sim$10 nM) to $\sim$4 mM in the SMTZ and then decrease slowly to $\sim$3 mM by 4.5 m (Fig. 2). ACP controls the shape of this profile (see Section 4b).

b. Pore-water property-property plots

A property-property plot of DIC and sulfate concentrations (Fig. 3) can be used to examine both the stoichiometry of sulfate reduction (Burdige 2006) and other dynamics of carbon cycling in these sediments (Burdige and Komada 2011). Taken at face value, the slope of this plot predicts an apparent carbon-to-sulfate ratio ($r_{C:S}$) for organoclastic sulfate reduction

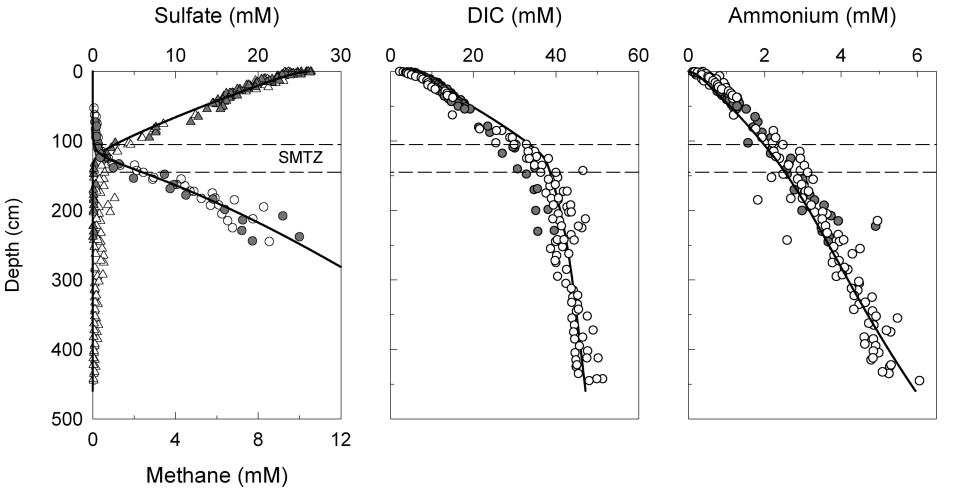

Figure 1. Depth profiles of pore-water sulfate, methane, dissolved inorganic carbon (DIC), and ammonium concentrations in Santa Barbara Basin sediments (data from Komada et al. 2016). In all panels, filled-in symbols are 2012 data, open symbols are 2013 data, and samples from each year represent data from several cores (multicores and gravity cores). In the left panel, sulfate symbols are triangles, whereas methane symbols are circles. In all three panels, the solid lines represent the best fit of the organic matter/methane/sulfate/ammonium (OMSN) model to the data (Section 4.c). The horizontal dashed lines here and in all other figures represent the upper and lower limits of the sulfate-methane transition zone (SMTZ) as defined in Komada et al. (2016).

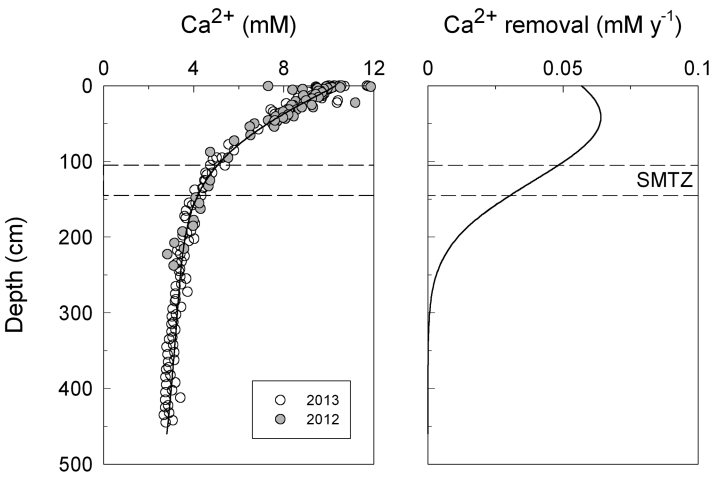

Figure 2. Left panel: Depth profiles of pore-water Ca^{2+} concentrations in Santa Barbara Basin sediments (data from Komada et al. 2016). The solid line represents the best fit of the organic matter/methane/sulfate/ammonium (OMSN) model to the Ca^{2+} data (Section 4.b). Right panel: The best-fit depth profile of Ca^{2+} removal from these sediment pore waters (i.e., the function $ACP(z)$ in equation 10). ACP, authigenic carbonate precipitation; SMTZ, sulfate-methane transition zone.

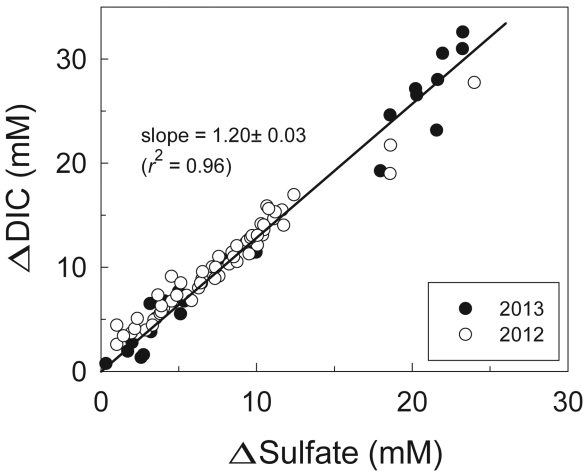

Figure 3. A DIC:sulfate pore-water property-property plot for cores collected in Santa Barbara Basin (data from Komada et al. 2016). Different symbols represent data from different years, and the "Δ" concentrations are relative to bottom-water values. The slope of the best-fit line through the data, $d(\Delta DIC)/d(\Delta Sulfate)$, is used to calculate $r_{C:S}$ (carbon-to-sulfate ratio for organoclastic sulfate reduction) with

$$\frac{d(\Delta DIC)}{d(\Delta Sulfate)} = r_{C:S}\frac{D_S}{D_{DIC}}$$

(Burdige 2006; Burdige and Komada 2011), where the two diffusion coefficients were taken from Table 3. Using these three quantities, the value of $r_{C:S}$ is 1.28 ± 0.04. The reported error is based on the slope of this line and assumed random errors in the diffusion coefficients. If we assume that there is a maximum ±2°C uncertainty in the bottom-water temperature at this site, this results in a 7% to 8% uncertainty in each diffusion coefficient based the temperature dependences of each D value (Schulz and Zabel 2006). However, this actually results in a <1% uncertainty in the diffusion coefficient ratio used in the calculation of $r_{C:S}$ because of the covariance of the two diffusion coefficients (i.e., changes in both D's are not independent of one another because of their common dependence on temperature). For DIC, we also assume that there is an additional 2.5% uncertainty in the DIC diffusion coefficient based on differences in the diffusion coefficients of the solutes that make up DIC (bicarbonate, carbonate, and aqueous CO_2) and a rough approximation of their contributions to the pore-water DIC pool (∼90%, 5%, and 5%, respectively; see, e.g., Komada et al. 2013). DIC, dissolved inorganic carbon.

(oSR) equal to 1.28 ± 0.04. If CH_2O organic matter (with a carbon oxidation state, ox, equal to zero) undergoes remineralization, the value of $r_{C:S}$ should be 2 (see Table 1), whereas if the organic matter undergoing remineralization is more reduced ($ox = -0.5$ to -0.7), this ratio will be lowered to 1.7 to 1.8. In many coastal and continental margin sediments (Jahnke 1990; Jørgensen and Parkes 2010; Burdige and Komada 2011), including those in SBB (Berelson et al. 2005), property-property plots yield apparent $r_{C:S}$ values that are lower than 2 (or even 1.7).

By itself, a value of $r_{C:S}$ equal to ~1.3 would require the remineralization of extremely reduced POC by oSR, with a carbon oxidation state of −2.2, a value approaching that of long chain hydrocarbons. For sediments in which the organic matter being remineralized is supplied to the sediments primarily by deposition at the sediment surface, it is difficult to envision a situation in which such extremely reduced organic matter is added to the sediments in any significant amount.

Authigenic carbonate precipitation = may explain some, but not all, of the observed discrepancy in this apparent $r_{C:S}$ value (also see Section 5c), although as we have shown previously (Burdige and Komada 2011), we believe that an explanation of these observations in nearby SMB sediments involves a deep "external" source of methane (which has a carbon oxidation state of −4) that is not directly coupled to present-day organic carbon deposition and burial and in situ methanogenesis. As in SMB sediments, the occurrence in SBB sediments of oSR with an $r_{C:S}$ value of ~1.7 and AOM (driven by an external methane source) with an $r_{C:S}$ value of 1 can result in intermediate values of $r_{C:S}$ such as is seen in Figure 3. Consistent with this explanation, sediments in both SBB and SMB are known to be sites of methane gas deposits and gas hydrates (Hill, Kennett, and Spero 2004; Hein et al. 2006; Leifer et al. 2006; Normark, Piper, and Sliter 2006; Paull et al. 2008). The fact that we can think about such a deep methane source as being uncoupled from contemporaneous surface organic carbon fluxes and any associated in situ methanogenesis will also be important in the development of the model presented subsequently.

4. Description of the model

a. Equations and numerical solutions

The organic matter/methane/sulfate/ammonium (OMSN) model is a steady-state reaction-transport model for pore-water sulfate (S), DIC (DIC), methane (M), ammonium (A), calcium (Ca), and reactive POC (G). These and all variables used in the model equations are defined in Table 2. This model is based on a similar model presented in Burdige and Komada (2013), although there are four fundamental changes to the model presented here.

First, we assume there are three pools (rather than one pool) of reactive organic matter that undergo remineralization at different rates in the sediments. Second, this model explicitly accounts for authigenic carbonate precipitation in the sediments. Third, depth-dependent porosity is now included in model equations, in part to account for the impact of the steep porosity gradient near the sediment surface (because of sediment compaction) on solid phase POC profiles. Finally, model equations also explicitly account for pore-water advection because of sedimentation and compaction. In contrast to models that examine sediment depths less than ~1 m (typical of many early diagenesis studies), a Peclet number analysis of the relative importance of pore-water advection versus diffusion (Burdige 2006) indicates that pore-water advection in SBB sediments is of sufficient importance over the length of the current model domain (4.6 m) to be included in these calculations. Our porosity data (not shown here, but see Komada et al. 2016) were fit to an equation containing the sum of two exponential functions, yielding

$$\varphi(z) = 0.78 + 0.07e^{-0.174z} + 0.15e^{-0.006z}, \tag{1}$$

where φ_o (the porosity at the sediment-water interface) equals 0.99, and φ_∞ (the asymptotic porosity at depth in the sediments) equals 0.78.

The model equations include the transport processes diffusion, sediment burial, and pore-water advection driven by sedimentation and compaction. The biogeochemical reactions included in the model are listed in Table 1. With the exception of ACP, the kinetic expressions used in the model for these processes have been described previously (Burdige and Komada 2013).

For each of the three G_i fractions of solid phase POC, the model equations were

$$\frac{\partial G_i}{\partial t} = -\frac{1}{(1-\varphi)}\frac{\partial}{\partial z}(\omega(1-\varphi)G_i) - \frac{k_i G_i S}{K_m + S} - f_S k_i G_i, \tag{2}$$

where the terms on the right side of equation (2) represent (in order) advection driven by sediment burial (sedimentation), oSR, and methanogenesis. Note that f_S is a function that inhibits the occurrence of methanogenesis when sulfate concentrations are above some threshold value (see Appendix). These three G_i fractions are a subset of the total sediment POC pool, which also includes a "refractory" component that is nonmetabolizable over the time and depth scale of the model domain.

For pore-water sulfate, the model equation is

$$\frac{\partial S}{\partial t} = \frac{1}{\varphi}\frac{\partial}{\partial z}\left(\varphi D_s \frac{\partial S}{\partial z}\right) - \frac{1}{\varphi}\frac{\partial}{\partial z}(\varphi v S) - \sum_{i=1}^{3}\frac{k_i L_2 \Im G_i S}{K_m + S} - \frac{k_{aom} S M}{K_a + S}, \tag{3}$$

where the terms on the right side of equation (3) represent diffusion, advection driven by sedimentation and compaction, and reaction terms for oSR (for 3 G_i fractions) and AOM. Analogous diffusion and advection terms also appear in equations (4) to (6). For pore-water methane, we have

$$\frac{\partial M}{\partial t} = \frac{1}{\varphi}\frac{\partial}{\partial z}\left(\varphi D_s \frac{\partial M}{\partial z}\right) - \frac{1}{\varphi}\frac{\partial}{\partial z}(\varphi v M) + \sum_{i=1}^{3} f_s k_i L_2 \Im G_i - \frac{k_{aom} S M}{K_a + S}, \tag{4}$$

where the reaction terms are for methanogenesis (for 3 G_i fractions) and AOM. For pore-water DIC, we have

$$\begin{aligned}\frac{\partial DIC}{\partial t} = {} & \frac{1}{\varphi}\frac{\partial}{\partial z}\left(\varphi D_s \frac{\partial DIC}{\partial z}\right) - \frac{1}{\varphi}\frac{\partial}{\partial z}(\varphi v DIC) + \sum_{i=1}^{3}\frac{k_i \Im G_i S}{K_m + S} + \sum_{i=1}^{3} f_S k_i L_3 \Im G_i \\ & + \frac{k_{aom} S M}{K_a + S} - ACP(z),\end{aligned} \tag{5}$$

where the reaction terms are for oSR and methanogenesis (for 3 G_i fractions each), AOM, and ACP ($ACP(z)$; described in Section 4.b). For pore-water Ca^{2+}, the model equation is

$$\frac{\partial Ca}{\partial t} = \frac{1}{\varphi}\frac{\partial}{\partial z}\left(\varphi D_s \frac{\partial Ca}{\partial z}\right) - \frac{1}{\varphi}\frac{\partial}{\partial z}(\varphi v Ca) - ACP(z), \tag{6}$$

where the sole reaction term is ACP.

For ammonium, the inclusion of pore-water advection driven by sedimentation and compaction requires that we also include reversible ammonium adsorption in the pore-water ammonium RT equation. Inclusion of adsorption results in a slightly more complex equation as compared with the ones presented previously, and the derivation of this equation is presented in the Appendix.

To solve these equations, we chose to first expand the complex spatial derivatives in each equation. The spatial derivative in the G_i equations and the spatial derivative for the diffusive term in the pore-water equations were expanded as described previously (Burdige and Komada 2011; 2013). The spatial derivative for the advective term in the pore-water equations was expanded as described in Burdige (2006; equations 6.15–6.19). For a general solute C,

$$\frac{1}{\varphi}\frac{\partial}{\partial z}(\nu\varphi C) = \frac{\varphi_\infty \omega_\infty}{\varphi}\frac{\partial C}{\partial z} = \frac{W}{\varphi}\frac{\partial C}{\partial z}, \tag{7}$$

where

$$W \equiv \varphi_\infty \omega_\infty = \frac{\varphi_\infty F_{sed}}{\rho_{ds}(1-\varphi_\infty)}, \tag{8}$$

Note the W/φ has units of sediment burial (e.g., cm y^{-1}).

After expansion of these derivatives, model equations were solved numerically using the Method-of-Lines technique with variable grid spacing (Schiesser 1991; Boudreau 1997; Burdige and Komada 2011). We used a fine grid spacing ($\Delta z = 0.05$ cm) near the sediment-water interface (0–0.5 cm) to better capture the details of the profiles in the near-surface sediments, gradually increased the grid spacing to 0.5 cm down to just below the SMTZ ($\sim$160 cm), and then further increased the grid spacing (to 9 cm) over the rest of the model domain (down to 4.6 m). A centered-finite-differencing scheme was used to approximate the first and second spatial derivatives in the solute equations (Boudreau 1997). In previous work (Burdige and Komada 2011), we used a backward differencing scheme to approximate the first spatial derivative in the solid (G_i) equations. However, here we have used a modified form of the centered-differencing leapfrog scheme (Boudreau 1997) that accounts for the variable grid spacing:

$$\left.\frac{\partial G}{\partial z}\right|_{z(i)} = \frac{G(i-1) - G(i-1)}{(\Delta z(i+1) + \Delta z(i))}, \tag{9}$$

where $\Delta z(i) = z(i) - z(i-1)$. This approximation of these derivatives greatly improves the accuracy of the calculations.

With this approach, the model equations for the four pore-water solutes and three G_i fractions were transformed from seven space- and time-dependent partial differential equations into a set of time-dependent ordinary differential equations (ODEs) valid at each grid point of the model domain. The Ca^{2+} equations were first solved separately to determine *ACP*(z), which is used in the DIC equations. This was done by fitting the numerical solution

of equation (6) to the Ca^{2+} pore-water data, as described in the next section. The set of the remaining coupled, nonlinear ODEs contains ~1,000–3,000 equations (i.e., n [typically 200–400] grid points over the model domain × 6 solutes and solids). This set of equations was solved to steady state in MATLAB using the integration package *ode15s* (note that a copy of the complete MATLAB script is available from the corresponding author).

In the integration package *ode15s*, the solver must determine the Jacobian matrix of the matrix of ODEs as part of the solution (Shampine and Reichelt 1997). The Jacobian matrix of this system of ODEs is a square matrix the size of the number of equations and therefore is quite large (up to 3,000 × 3,000 entries; see paragraph above). It is also generally very sparse, having >95% zero elements. Specifying the pattern of the Jacobian matrix in the MATLAB script (using the MATLAB function *Jpattern*) thus greatly speeds up the calculations. By specifying the pattern of this matrix, the solver only attempts to numerically estimate the value of an element in the matrix that is nonzero (for details also see MathWorks 2016a, 2016b).

b. Determination of ACP*(z) using pore-water* Ca^{2+} *data*

Pore-water profiles of Ca^{2+}in SBB sediments determined here (Fig. 2) and in earlier studies (Sholkovitz 1973; Reimers et al. 1996; Berelson et al. 2005) all show decreases with sediment depth, which have been interpreted as being the result of ACP. Solubility calculations with our data (results not shown here) show that SBB sediments are supersaturated with respect to calcium carbonate over the entire model domain (0–4.6 m), consistent with calculations presented in Reimers et al. (1996), whose studies of surface SBB sediments (0–8 cm) show that these sediments become supersaturated with respect to calcite a few millimeters below the sediment-water interface.

In our work, rather than using a formal kinetic rate expression for ACP in the RT equation for Ca^{2+} (e.g., Morse, Gledhill, and Millero 2003), we chose to assume that a Gaussian function could be used to define the depth distribution of ACP:

$$ACP(z) = R_{\max} e^{-0.5[(z_{cp}-z)/s_{cp}]^2}. \tag{10}$$

This formulation was based, in part, on studies of other sedimentary systems that have suggested that ACP may be focused around the SMTZ (i.e., here z_{cp} would be close to the depth of the SMTZ) because of alkalinity production by AOM in this region (e.g., see discussions in Reeburgh 2007; Chatterjee et al. 2011).

With the inclusion of this mathematical formulation for $ACP(z)$ into equation (6), the numerical solution of the equation was fit to the Ca^{2+} pore-water data by varying $R_{\max}$, z_{CP}, s_{cp}, and J_{lbCa} to minimize the error of the fit. This was done in MATLAB using the routine *fminsearch*. In this solution, the bottom-water Ca^{2+} concentration was used as the boundary condition of the model equation at $z = 0$ cm (Table 3), and a flux boundary condition was used at the base of the model.

Table 3. Diffusion coefficients and bottom-water concentrations.

Solute	D^o (cm^2 y^{-1}) [a]	C^o (mM) [b]
Ca^{2+}	134.2	10.3
Dissolved inorganic carbon (HCO_3^-)	192.1	2.3
Methane	275.2	0 [c]
NH_4^+	346.9	0.002
SO_4^{2-}	180.3	26.2

[a] Seawater, free solution diffusion coefficients at 5°C (bottom-water temperature). Taken from Schulz and Zabel (2006).
[b] Except where noted, C° is the average bottom-water concentration measured in hydrocast samples.
[c] Assumed bottom-water value.

Table 4. Summary of fitting results.

Parameter	Best-fit value	Units
G_1^o	0.86 ± 0.16	wt%
G_2^o	0.64 ± 0.26	wt%
G_3^o	0.64 ± 0.07	wt%
k_1	0.54 ± 0.10	y^{-1}
k_2	0.17 ± 0.04	y^{-1}
k_3	$2.5 \pm 1.0 \times 10^{-3}$	y^{-1}
k_{aom}	4.98 ± 1.50	mM^{-1}y^{-1}
r_{NC1}	6.9 ± 0.9	mol mol^{-1}
r_{NC2}	8.0 ± 1.1	mol mol^{-1}
r_{NC3}	10.3 ± 1.4	mol mol^{-1}
J_{lbM}	-0.243 ± 0.059	mmol m^{-2} d^{-1}
J_{lbDIC}	-0.054 ± 0.016	mmol m^{-2} d^{-1}
J_{lbA}	-0.062 ± 0.012	mmol m^{-2} d^{-1}
K_{in}	0.20 ± 0.04	mM
S^*	0.98 ± 0.16	mM
R_{max}	0.064	mM y^{-1}
z_{cp}	41.4	cm
s_{cp}	84.7	cm

All errors are 1 standard deviation. See Table 2 for definitions of parameters.

The resulting best-fit to the Ca^{2+} pore-water data and the associated depth distribution of $ACP(z)$ are shown in Figure 2. Table 4 contains the best-fit parameters. Here, we see that instead of ACP being narrowly focused around the SMTZ, the process is broadly centered at ~60 cm above the SMTZ ($z_{cp} = 41$ cm), roughly in the region where the Ca^{2+} pore-water gradient is the steepest.

An attempt was also made to fit the Ca^{2+} data by assuming that the function $ACP(z)$ could be defined as a series of equally spaced regions between 0 and 300 cm, each with a constant (but possibly different) rate of carbonate precipitation. When $ACP(z)$ consisted of five such

regions, this yielded a Ca^{2+} profile that was indistinguishable from the one in Figure 2, and an $ACP(z)$ depth profile whose general shape was similar to that of the best-fit Gaussian curve in this figure. Both approaches also resulted in essentially the same depth-integrated rate of ACP (0.22 and 0.21 mmol m^{-2} d^{-1} for the Gaussian and step functions, respectively). Attempts to better define a step function distribution of $ACP(z)$ using a larger number of narrower depth zones resulted in what appeared to be an unrealistic depth distribution of this function (i.e., alternating very high and very negative or near-zero rates of carbonate precipitation).

c. Fitting the OMSN model to the pore-water data

Using this depth distribution of $ACP(z)$, the OMSN model was fit to the pore-water profiles of methane, sulfate, DIC, and ammonium as follows. Known bottom-water concentrations were used as the upper boundary condition of the model equations at $z = 0$ cm (Table 3), and a flux boundary condition was used at the base of the model. For methane, DIC, and ammonium, these diffusive fluxes were used as adjustable parameters in the fitting process, whereas for sulfate this flux was assumed to be equal to zero.

In fitting the methane data with the OMSN model, we also note that almost all of the in situ pore-water methane concentrations below the SMTZ exceed saturation values at 1 atm. As a result, methane degassing during core processing and sampling can lead to measured concentrations being lower than their in situ values (e.g., Lapham et al. 2010). Based on arguments presented in Komada et al. (2016), the methane data we used in our fitting (Fig. 1) represent a subset of all our measured methane concentrations (mostly values from sediment depths above 200 cm) that we believe are least affected by degassing.

The numerical solution of the OMSN model equations was then fit to the sulfate, ammonium, DIC, and methane pore-water data by varying S^* and K_{in} (from the expression for f_S; see equation A1), along with k_{aom}, J_{lbM}, J_{lbDIC}, and J_{lbA}, plus the three values each of k_i, G_i^o, and r_{NCi} (15 fitting parameters in total; see Table 4). The best fit of the model to the depth profiles of all four solutes was obtained by varying these fitting parameters to minimize the average of the four errors ($1 - r^2$) for each fit (referred to here as *err*). This was carried out in MATLAB using the routine *lsqnonlin*.

Given the large number of fitting parameters in the model, it was important to ensure that the fitting process found a global (vs. local) minimum value of *err*. This was carried out using a Monte Carlo approach, which also allowed us to estimate the uncertainty of the fitting parameters in Table 4. Beginning with a set of values for these fitting parameters that resulted in a reasonable (eyeball) fit to the data, each of these values was randomly varied by up to ±50%, and they were then used as a set of starting values in *lsqnonlin* to obtain a new set of best-fit values for the fitting parameters. This entire process was repeated >50 times. Except for an occasional fit that failed to converge to a stable solution, all other fits converged to stable solutions with a value of *err* that was less than 0.05 (roughly equivalent to an average r^2 value of 0.95 for the fits to the four profiles).

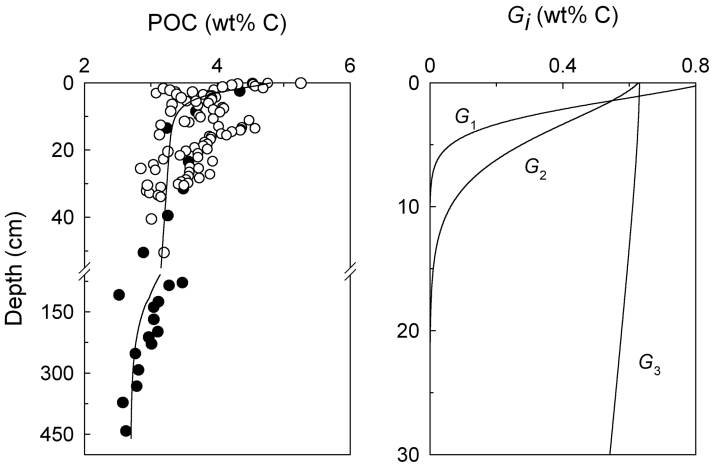

Figure 4. Left panel: Depth profile of solid phase particulate organic carbon (POC) concentrations in Santa Barbara Basin sediments. Black circles are 2012 and 2013 data from Komada et al. (2016), whereas open circles are from cores collected in 1988 (Reimers et al. 1996). Also shown here are depth profiles of the best-fit, model-determined reactive POC concentrations ($\sum G_m = G_1 + G_2 + G_3$) with 2.7 wt% C arbitrarily added to the model results. As discussed in Section 5, this may represent organic carbon that is nonmetabolizable over the depth scale of this profile. Also note that the model results shown here were not generated by fitting the organic matter/methane/sulfate/ammonium (OMSN) model to the POC data but were independently calculated with best-fit results from the fit of the OMSN model to the pore-water data listed in Table 4. Right panel: Model-determined concentrations of reactive organic carbon in the G_1, G_2, and G_3 fractions based on results from the OMSN model fit (Section 4c).

5. Discussion

The results in Table 4 represent averages and ±1 standard deviation (σ) of the fitting parameters from fits that satisfied the criteria described previously. Values in this table gave very good fits to all of the data (Fig. 1); the r^2 values for the sulfate, DIC, ammonium, and methane fits were 0.990, 0.976, 0.953, and 0.962, respectively.

As a further test of the OMSN model results, we took the model-derived depth profiles of reactive organic matter (i.e., the sum of the three G_i fractions = $\sum G_m$) and compared them with our measured POC values (Komada et al. 2016) and those in Reimers et al. (1996). We see (Fig. 4) that if ~2.7 wt% C is added to the values of $\sum G_m$—and we think of this as organic carbon that is nonmetabolizable over the depth scale of this profile—then this model-derived POC profile is remarkably consistent with the data. Note that this result was not obtained by fitting the OMSN model to the POC data but was obtained after the fact using parameters derived from independently fitting the model to the inorganic pore-water depth profiles. The organic carbon content of sinking particles in SBB ranges from ~3 to

7 wt% C (Thunell 1998), which also agrees well with the measured and modeled surface sediment POC concentrations in Figure 4.

The values of r_{CN1} and r_{CN2} are both between ~7 and 8 (Table 4) and are consistent with a marine source for the G_1 and G_2 organic matter fractions. They are in general agreement with values of the C:N ratio of organic matter in sinking particles in the basin (range = 7–8.5; Thunell 1998). Prokopenko et al. (2006) similarly concluded that marine organic matter dominates the organic matter undergoing remineralization in SBB sediments, based on pore-water concentration property-property plots and studies of $\delta^{15}N$ of pore-water ammonium. The model-derived G_3 organic matter fraction has a higher C:N ratio (r_{CN3} ~10) than the other two fractions. One possible explanation for the source of this material is lateral downslope transport of preaged (and partially degraded) marine organic matter (Hwang, Druffel, and Komada 2005; Mollenhauer and Eglinton 2007).

a. Organic matter remineralization rate constants

The k_i values obtained here (Table 4) are within the range of values observed in other continental margin sediments (Middelburg 1989; Boudreau 1997; Arndt et al. 2013), including those that we have determined for SMB sediments (Komada et al. 2013). When we directly compare SMB and SBB k_i values, we see that k_1 in SBB sediments (~0.4–0.6 y^{-1}) is much larger than k_1 in SMB sediments (0.02–0.1 y^{-1}), although k_1 in SMB sediments is more similar to k_2 in SBB sediments (0.1–0.2 y^{-1}). In addition, k_2 in SMB sediments and k_3 in SBB sediments are both similar in magnitude (0.004–0.07 y^{-1} and 0.001–0.003 y^{-1}, respectively). The faster sedimentation rate in SBB versus SMB (0.1 vs. 0.013 g cm^{-2} y^{-1}; see Table 2 and Christensen et al. 1994), may allow us to better "see" the degradation of a more reactive type of organic matter in SBB sediments. There may also simply be a greater input of more reactive organic matter to these sediments. These observations also point out that a comparison of organic matter reactivity in different sediments is very much a function of the timescales of the observations (e.g., Hedges and Keil 1995; Burdige 2006). From the perspective of the power law for organic matter reactivity (Middelburg 1989), it indicates that the bulk reactivity of sediment organic matter scales inversely with the age of the organic matter.

Such differences among degradation rate constant values have also been examined in terms of how these values vary as a function of "global" parameters such as water depth, sedimentation rate, or organic matter flux to the sediments (for a recent review see Arndt et al. 2013). Other formulations allow for these k values (i.e., POC reactivity) to be viewed as a continuous function of the age of the material and, therefore, depth in a sediment column (Middelburg 1989; Boudreau and Ruddick 1991). However, given our interest in linking the results of modeling studies such as this one to models of dissolved organic matter cycling in sediments (Komada et al. 2013), we find it more straightforward to use a multi-G approach (Westrich and Berner 1984; Burdige 1991) to parameterize the changing properties (e.g., isotopic or chemical composition) of sediment organic matter undergoing remineralization beyond its bulk reactivity.

Table 5. Depth-integrated rates of organoclastic sulfate reduction (*DI-oSR*) [a], anaerobic oxidation of methane (*DI-AOM*) [a], methane production (*DI-MP*) [a], and authigenic carbonate precipitation (*DI-ACP*) [b].

Depth range (cm)	*DI-oSR*		*DI-AOM*		*DI-MP*		$DI-ACP$		$\frac{Sulfate\ flux}{Methane\ flux}$ [c]
0–40	2.13	(86%)					0.06	(27%)	
40–105	0.28	(11%)	0.04	(8%)			0.09	(41%)	
105–145 (SMTZ)	0.06	(3%)	0.47	(91%)	0.08	(21%)	0.04	(16%)	1.4
>145			<0.01	(1%)	0.30	(79%)	0.03	(15%)	
Total	2.48	(100%)	0.51	(100%)	0.38	(100%)	0.22	(100%)	

[a] *DI-oSR* has units of mmol S m^{-2} d^{-1}, and *DI-MP* has units of mmol CH_4 m^{-2} d^{-1}. Given the stoichiometry of AOM, the value here of *DI-AOM* is the same with either set of units. As discussed in the text (Section 4a), the rates of oSR, AOM, and MP are expressed as follows:

$$oSR = \sum_{i=1}^{3} \frac{k_i L_2 \Im G_i S}{K_m + S} \qquad AOM = \frac{k_m SM}{K_a + S} \qquad MP = \sum_{i=1}^{3} f_S k_i L_2 \Im G_i,$$

with units of mM y^{-1}. Using the organic matter/methane/sulfate/ammonium model–derived best-fit depth profiles of $G_i (i = 1 - 3$; see Fig. 4), sulfate (S; see Fig. 1), and methane (M; see Fig. 1), depth profiles of these rates were determined (see Fig. 5), multiplied by φ (see equation 1), and then depth-integrated (by trapezoidal approximations) for each of the depth ranges.

[b] *DI-ACP* has units of mmol Ca m^{-2} d^{-1} or mmol C m^{-2} d^{-1}. The rate of ACP is given by equation (10), and using the model-derived values in Table 4, depth profiles of this rate were determined (see Fig. 2), multiplied by φ, and then depth-integrated (by trapezoidal approximations) for each of the depth ranges.

[c] The ratio of the downward sulfate flux into the sulfate-methane transition zone (SMTZ) to the upward methane flux into the SMTZ. The sulfate flux into the SMTZ was determined here as the sum of *DI-oSR* and *DI-AOM* in the SMTZ (=0.53 mmol S m^{-2} d^{-1}). The methane flux into the SMTZ was determined here as the difference between *DI-AOM* and *DI-MP* in the SMTZ (=0.39 mol CH_4 m^{-2} y^{-1}).

b. Sulfate reduction rates and remineralization processes in the sulfate zone and the SMTZ

The depth-integrated rate of sulfate reduction directly determined for the upper 40 cm of SBB sediments, 2.14 mmol S m^{-2} d^{-1} (Reimers et al. 1996), agrees very well with the depth-integrated sulfate reduction rate for this depth interval determined with the OMSN model (2.13 mol S m^{-2} y^{-1}; Table 5). Dividing sulfate reduction into oSR and AOM, we see that although the vast majority of oSR occurs above 40 cm (86%), it continues on into the deeper sediments and into the SMTZ (below 105 cm), where it then co-occurs with AOM (also see Fig. 5).

As shown in Figure 1 and discussed in earlier works (Berelson et al. 2005; Harrison et al. 2009; Komada et al. 2016), sulfate profiles in SBB sediments (and other continental margin sediments) are highly linear below ~10–20 cm down to the SMTZ. Linear sulfate profiles below this surface zone where oSR is active may occur when sulfate diffuses downward with no in situ consumption by oSR until sulfate is consumed by AOM in the SMTZ. This would imply that POC buried below this surface region is nonreactive toward degradation by oSR, and it would also suggest that there should be a 1:1 ratio between the downward

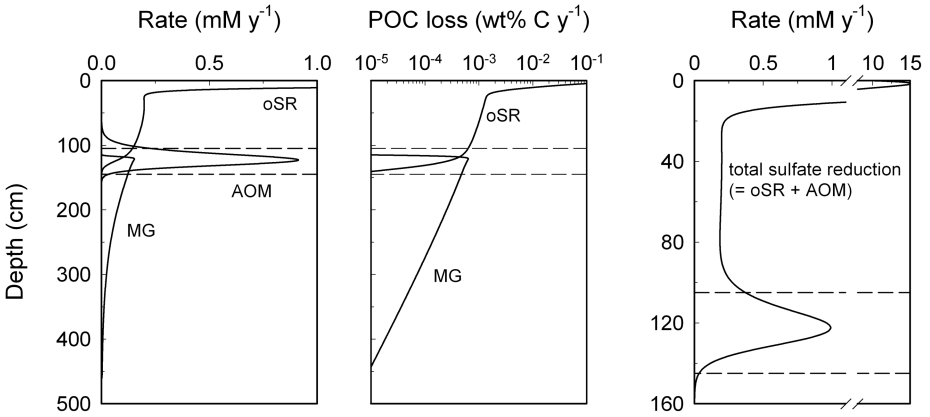

Figure 5. Left panel: Depth profiles of model-determined rates of organoclastic sulfate reduction (oSR), anaerobic oxidation of methane (AOM), and methanogenesis (MG). These rate profiles were determined using best-fit depth profiles of sulfate and methane, model-derived profiles of $G_i (i = 1 - 3)$, as shown in Figure 4, and rate expressions listed in the Table 5 notes (also see equations 2–4 in the text). The dashed lines represent the upper and lower limits of the sulfate-methane transition zone (SMTZ) as defined in Komada et al. (2016). Center panel: Depth profiles of the rates of oSR and MG from the panel on the left reexpressed as the rate of particulate organic carbon (POC) loss. Note that with the exception of the transition from oSR to MG in the SMTZ, there is a near-continuous decline in POC loss through the entire sediment column. The sharp drop-off in oSR in the SMTZ is likely due in part to competition for sulfate between oSR and AOM. In addition, the change in slope in the oSR depth profile below ~20 cm occurs because of the near-complete depletion of G_2 organic matter, and the fact that G_3 organic matter is much less reactive (see Table 4). Right panel: Depth profile of the rate of total sulfate reduction (= oSR+AOM) in the upper 160 cm of sediment. Note the different depth scale in this panel. Also note the high rate of sulfate reduction near sediment surface (exclusively oSR); the low, but nonzero, rates of sulfate reduction between ~20 cm and the top of the SMTZ (105 cm); and the subsequent ~4- to 5-fold increase in the rate of sulfate reduction (mostly AOM) in the SMTZ.

sulfate flux and the upward methane flux into the SMTZ, given the stoichiometry of AOM (Table 1).

However, imbalances between the downward sulfate flux and the upward methane flux into the SMTZ (i.e., sulfate-to-methane flux ratio >1) imply that oSR and AOM must be occurring in the SMTZ (Berelson et al. 2005; Komada et al. 2016). This then appears to result in the following conundrum: organic matter that appears to be refractory toward oSR in a region below the sediment surface where sulfate is still abundant becomes reactive again to sulfate reduction with burial deeper in the sediments in the SMTZ, at low sulfate levels. This material then also continues to be reactive toward methanogenesis below the SMTZ. The causes of this are not well understood or explained, although it has been suggested that it may be the result of a priming effect (Canfield 1994; Bianchi 2011) in which AOM

stimulates (in some way) the oxidation of this refractory POC (by oSR) in the SMTZ (Berelson et al. 2005).

The results presented here and modeling results in Burdige and Komada (2011) provide another possible explanation for the sulfate pore-water profile. In Figure 5, we see that there are high rates of sulfate reduction (as oSR) near the sediment surface and a second peak in the sulfate reduction rate in the SMTZ (largely as AOM) with low (but nonzero) rates of oSR in the intermediate region in-between. Here, this also results in a linear sulfate profile (Fig. 1) and gives the appearance of refractory POC burial and conservative behavior of sulfate between the sediment surface and the SMTZ. Downward pore-water advection by compaction and sedimentation may also play a role in explaining these linear sulfate profiles by compensating for any slight sulfate depletion (by oSR) in this intermediate region. A decrease with depth in sulfate diffusivity because of decreasing porosity may have a similar effect on sulfate concentrations in this region (Lerman 1977; Dickens 2001).

Despite the apparent linearity of the sulfate profile, if we express the rates of oSR and methanogenesis as the rate of POC loss (based on the stoichiometry illustrated in Table 1), there is a near-continuous decline in the rate of POC loss by the two processes over the entire sediment column (Fig. 5), interrupted only in the SMTZ by the transition between oSR and methanogenesis and the occurrence of AOM (and therefore competition for sulfate between oSR and AOM). The sharp rate transition in the upper sediments (∼20 cm) is driven by the fact that the k value for G_3 organic matter remineralization is roughly two orders of magnitude smaller than the k values for the remineralization of G_1 and G_2 organic matter (Table 4).

In Table 5, we used model-derived depth-integrated rates in the SMTZ to define a quantity that is functionally equivalent to the sulfate-to-methane flux ratio into the SMTZ. Using this approach, this "flux" ratio is 1.4. Using the same data set we modeled here, Komada et al. (2016) directly estimated this ratio with diffusive fluxes derived from linear fits to the sulfate data above the SMTZ and the methane data below the SMTZ. Their ratio (∼1.7–2) is similar to, though somewhat higher, than the value estimated here. Despite these differences, both sets of results are consistent with similar results in Berelson et al. (2005) regarding the co-occurrence of oSR and AOM in the SMTZ of SBB sediments.

c. A carbon budget for SBB sediments and the significance of deep methane fluxes

In Table 6, we use our model results to calculate a carbon budget for SBB sediments. An examination of this budget indicates that there are opposing advective and diffusive fluxes for the solutes DIC, methane, and ammonium (not shown here) at the lower boundary of the sediment model domain. Over smaller sediment length scales and for lower sedimentation rates, pore-water advection and burial are generally small and can be ignored (see Section 4.a), although here they are of greater importance. For DIC, we see that downward burial at the lower boundary exceeds the upward basal diffusive flux, whereas while for methane the upward methane diffusive flux is larger than the downward burial flux.

Table 6. A reduced carbon budget for Santa Barbara Basin sediments.

Process	Value (mmol C m^{-2} d^{-1})
Inputs	
Reactive particulate organic carbon (POC) [a]	4.80
Upward basal diffusive methane flux (J_{lbM}) [b]	0.24
Upward basal diffusive dissolved inorganic carbon (DIC) flux (J_{lbDIC}) [b]	0.05
Total	5.09
Removal	
DIC benthic flux [c]	4.62
Basal DIC burial [d]	0.17
Basal methane burial [e]	0.08
Authigenic carbonate precipitation (*DI-ACP*) [f]	0.22
Total	5.09

[a] Determined as $F_{sed} \cdot (G_1^o + G_2^o + G_3^o)$. Because >99.5% of all reactive POC deposited in these sediments is remineralized over the 4.6 m sediment model domain, we have neglected this small loss term in these calculations.
[b] From Table 4.
[c] Diffusive fluxes (J) across the sediment-water interface were calculated using Fick's first law modified for sediments (e.g., Burdige 2006):

$$J = -\varphi_o D_x^s \left.\frac{dC}{dZ}\right|_o ,$$

where φ_o equals 0.99 (see equation 1), and D_x^s is the bulk sediment diffusion coefficient for species x (Table 3). Using model results, the concentration gradient at the sediment-water interface, $dC/dz|_o$, is approximated as $\Delta C/\Delta z$, where ΔC is the concentration difference between the concentration value at the first model grid point and the concentration in the overlying waters (Table 3), and Δz is the depth of the first grid point.
[d] The downward burial of pore-water DIC is defined as $\nu_n \varphi_n DIC(n)$, where $DIC(n)$ is the DIC concentration at the last (basal) grid point, and the subscript n indicates that these are values of the porosity and rate of pore-water advection at depth $z(n)$. The term $\nu_n \varphi_n$ equals W (see equation 8) because $\varphi_n \nu_n = \varphi_\infty \nu_\infty = \varphi_\infty \omega_\infty = W$ based on equations 6.15–6.19 in Burdige (2006).
[e] The downward burial of pore-water methane is defined as $\nu_n \varphi_n M(n)$, where the first two terms here are defined as described in the previous note, and $M(n)$ is the methane concentration at the last (basal) grid point.
[f] From Table 5.

Although the upward flux of methane is only ~5% of the input of reactive POC at the sediment surface (Table 6), it is close to three-quarters that of the depth-integrated rate of methane production in the model domain (Table 5). This then results in the depth-integrated rate of AOM being greater than the depth-integrated rate of methane production and suggests that this upward methane flux (which makes up the difference between AOM and in situ methanogenesis) plays an important role in the biogeochemical dynamics of the SMTZ.

Along with ACP, this additional basal source of methane contributes to the low apparent $r_{C:S}$ value in Figure 3 (also see Section 3b). Again, it is important to note here that this upward methane flux must be uncoupled from present-day organic carbon deposition and burial,

along with remineralization processes in the sediments above the lower model boundary (i.e., in situ methanogenesis), because AOM driven solely by in situ methanogenesis will not result in such apparent low $r_{C:S}$ values in property-property plots (Burdige and Komada 2011).

As discussed previously, methane derived from the decomposition of deep gas hydrates will be uncoupled from present-day organic carbon deposition and burial. However, another source of methane that may be uncoupled from modern organic carbon input is biogenic (or perhaps thermogenic) methane production hundreds of meters below the seafloor. This type of methane production is common in some outer continental margin/continental slope sediments and appears to be stimulated by increasing sediment temperatures associated with the sediment geothermal gradient (e.g.,Wellsbury et al. 1997; Parkes et al. 2007; Snyder et al. 2007; Burdige 2011).

Attempts to differentiate between these different methane sources are, however, equivocal based on the model-derived basal fluxes of methane (J_{lbM}), DIC (J_{lbDIC}), and ammonium (J_{lbA}). The ratio of the basal methane flux to the DIC flux ($J_{lbM}/J_{lbDIC} \approx 4.5$; see Table 4) would argue against the predominance of a deep biogenic source because such a deep source should result in a flux ratio close to 1, based on the stoichiometry of methanogenesis in Table 1. Although methane derived from a decomposing hydrate source is expected to have little accompanying DIC (see discussions in Burdige and Komada 2013), an upward flux of thermogenic methane not associated with a currently decomposing hydrate is also expected to have little accompanying DIC (Snyder et al. 2007). However, the nonzero value of the upward ammonium flux (J_{lbA}) argues against thermogenic methane production because at the temperatures of thermogenic methane production, ammonium is unstable and reacts with CO_2 to form methane and N_2 (Zhu, Shi, and Fang 2000). Little ammonium is also expected to accompany a methane flux from a decomposing deep hydrate (Burdige and Komada 2013). However, if we assume that the methane, DIC, and ammonium fluxes are initially the result of a deep biogenic source, and that the low DIC flux is the result of some accompanying deep uptake process, the total carbon remineralized by such a deep biogenic source should be roughly two times the upward methane flux ($\sim 2J_{lbM}$). This then further suggests that the C:N ratio of the organic matter being remineralized at depth by this high-temperature methanogenesis could be $\sim 2J_{lbM}/J_{lbA} = 7.8$, which does not appear to be an unreasonable value. More work will be needed to further explore the sources of this deep methane flux, and ongoing modeling studies of carbon isotopes (^{13}C and ^{14}C) in pore-water DIC and methane may shed light on this problem.

6. Conclusion

A modified RT model for anoxic marine sediments is described here and applied to data from sediment cores in SBB to a maximum sediment depth of 4.6 m. The major conclusions of the model results are:

1. Model fits are quite good and yield results (rate constants, depth-integrated rates of sulfate reduction) that agree with previous studies of SBB and other continental margin sediments.

2. Model-derived values of reactive organic carbon (i.e., $\sum G_m = G_1 + G_2 + G_3$) agree very well with measured POC values in SBB sediments if we assume that ~2.7 wt% C of the measured bulk POC in the sediments is nonmetabolizable.

3. Model results suggest that authigenic carbonate precipitation is not centered around the SMTZ but occurs at much shallower depths in the sediments and over a relatively broad sediment depth range.

4. The model-determined, depth-integrated rate of sulfate reduction (upper 40 cm) agrees extremely well with the directly determined value. Although the vast majority of oSR in model results occurs above 40 cm, oSR continues on into the deeper sediments and into the SMTZ, where it co-occurs with AOM. This co-occurrence of oSR and AOM is consistent with observations in the literature that the ratio of the downward sulfate flux and the upward methane flux into the SMTZ of SBB sediments is greater than 1.

5. The observed linear sulfate profile from just below the sediment surface to the SMTZ suggests the occurrence of conservative sulfate behavior and refractory POC burial in this region of the sediments. However, model results based on a fit to the sulfate data suggest that such linear profiles may also occur when high rates of sulfate reduction (as oSR) occur near the sediment surface and in the SMTZ (largely as AOM) with low, but nonzero, rates of oSR in-between. Linearity in the sulfate profile may also be related to the occurrence of downward pore-water advection by compaction and sedimentation, as well as a decrease with depth in sulfate diffusivity because of decreasing porosity.

6. The depth distribution of model-determined rates of oSR and methanogenesis results in a rate of POC loss that declines near-continuously in a logarithmic fashion over the entire sediment column.

7. The results presented here provide additional evidence for the fact that low apparent values of $r_{C:S}$ (based on a sulfate: DIC property-property plot) require an upward methane flux that is not directly coupled to present-day organic carbon deposition and burial and in situ methanogenesis. These methane sources may include deeply buried decomposing gas hydrates, which are common in many continental margin settings, or perhaps biogenic (or thermogenic) methane production hundreds of meters below the seafloor, stimulated by increasing sediment temperatures associated with the sediment geothermal gradient.

Acknowledgments. We thank all the people who assisted us in collection of the data we have examined here, including the captain and crew of R/V *Robert Gordon Sproul* and R/V *New Horizon* and Scripps Institution of Oceanography marine technicians L. Ellet and M. Donohue; the Oregon State University coring group and especially D. Hubbard; and J. Bleakney, A. Gerretson, A. Grose,

E. Harrison, A. K. Kada, H.-L. Li, G. Paris, B. Riegel, and P. Tennis who provided us with assistance in the field. Comments by Bernie Boudreau, Associate Editor Bob Aller, and an anonymous reviewer improved an earlier version of this manuscript. This work was supported by the National Science Foundation under grant numbers OCE-1155562 (DJB), OCE-1155764 (TK), and OCE-1155320 (JPC).

APPENDIX

a. Inhibition of methanogenesis when sulfate is present

A number of different empirical approaches have been used in models like the organic matter/methane/sulfate/ammonium (OMSN) model to inhibit the occurrence of less efficient (i.e., lower free energy yield) remineralization processes when more efficient (higher free energy yielding) electron acceptors are present. Here, specifically, this involves the inhibition of methanogenesis when sulfate is present above some threshold concentration. In past efforts (e.g., Burdige and Komada 2013) and in early work with the OMSN model, we used a function that equals 0 when sulfate concentrations are above a threshold concentration ($\sim 10^{-3}$ mM) and rapidly goes to 1 below this concentration. With this function, there is effectively no overlap between anaerobic oxidation of methane (AOM) and methane production (MP) (or between AOM and organoclastic sulfate reduction [oSR], for that matter). However, in the work described here and in modeling $\delta^{13}C_{DIC}$ and $\delta^{13}C_{CH4}$ profiles (D.J. Burdige, T. Komada, C. Magen, J.P. Chanton, unpublished), we observed that we were able to better fit the data by relaxing the requirement of a strict separation between sulfate reduction (i.e., AOM) and methanogenesis. This observation is also consistent with other studies, which have argued that the co-occurrence of AOM and methanogenesis in the sulfate-methane transition zone is a likely explanation for the extreme ^{13}C-depletion of methane found in this region of the sediments (e.g., Borowski, Paull, and Ussler 1997; Pohlman et al. 2008). Therefore, in this model, we defined f_S using this form of the complementary error function described previously in a similar model of coastal marine sediments (Martens, Albert, and Alperin 1998):

$$f_S = \frac{0.5}{\sqrt{\pi}} \int_S^{\infty} e^{-[(\zeta - S*)/K_{in})]^2} d\zeta \cong \begin{cases} 1 & if\ S < S* \\ 0 & if\ S > S* \end{cases}, \tag{A1}$$

where K_{in} controls the steepness of the transition of f_S from 0 to 1 that occurs around S^* (see, e.g., a plot in Martens, Albert, and Alperin 1998). Values for both K_{in} and $S*$ were obtained during the fitting of pore-water data to the OMSN model (see Section 4c). Note that this approach can also lead to a strict separation between MP and AOM and oSR for a value of S^* that is close to zero.

b. Derivation of the pore-water ammonium equation to account for reversible adsorption

In sediments where pore-water advection driven by burial and compaction cannot be (or is not) ignored, inclusion of reversible ammonium adsorption in reaction-transport equations

is a bit more complex than has been previously discussed (e.g., Berner 1976). If we make the common assumption that ammonium adsorption is rapid and reversible (i.e., at local equilibrium), then $\bar{A}$, the concentration of adsorbed ammonium (in units of, e.g., mmol g dwt^{-1}), equals K^*A, where K^* is the equilibrium adsorption coefficient, and the RT equation for pore-water ammonium can be written as follows (Berner 1976; Boudreau 1997):

$$\frac{\partial A}{\partial t} = \frac{1}{\varphi}\frac{\partial}{\partial z}\left(\varphi D_s \frac{\partial A}{\partial z}\right) - \frac{1}{\varphi}\frac{\partial}{\partial z}(\varphi v A) + R_{prdn} + R_{ads}, \tag{A2}$$

where for now the mathematical formulation of the ammonium production rate (R_{prdn}) is unspecified, as is the kinetics of reversible ammonium adsorption from the pore waters (R_{ads}). The reaction-transport equation for adsorbed ammonium is then written as

$$\frac{\partial \bar{A}}{\partial t} = -\frac{1}{(1-\varphi)}\frac{\partial}{\partial z}\left(\omega(1-\varphi)\bar{A}\right) + \overline{R}_{ads}, \tag{A3}$$

where $\overline{R}_{ads}$ is the rate of reversible ammonium adsorption from the solids. In an analogous fashion to $\Im$, we first define F_1 as $[(1–\varphi)/\varphi] \cdot 10^3 \cdot \rho_{\text{ds}}$, and to rearrange equation (A2) into a more tractable form for solving it, we multiply equation (A3) by F_1 and add it to equation (A2).

With this, the time derivatives on the left side of this modified form of equation (A2) become

$$\frac{\partial}{\partial t}(A + F_1\bar{A}) = \frac{\partial}{\partial t}(A + F_1 K^* A) = (1+K)\frac{\partial A}{\partial t}, \tag{A4}$$

where K, the dimensionless adsorption coefficient, equals $F_1 K*$ (Burdige 2006). Because we have assumed that adsorption is at local equilibrium, we do not have to specify the kinetic expressions for R_{ads} and $\bar{R}_{ads}$, but can simply recognize that $R_{ads} = -F_1 \cdot \bar{R}_{ads}$ (Berner 1976; Boudreau 1997). With this, the right side of this addition of equations (A2) and (A3) yields

$$\begin{aligned}(1+K)\frac{\partial A}{\partial t} &= \frac{1}{\varphi}\frac{\partial}{\partial z}\left(\varphi D_s \frac{\partial A}{\partial z}\right) - \frac{1}{\varphi}\frac{\partial}{\partial z}(\varphi v A) - \frac{F_1}{1-\varphi}\frac{\partial}{\partial z}(\omega(1-\varphi)\bar{A}) + R_{prdn} \\ &= \frac{1}{\varphi}\frac{\partial}{\partial z}\left(\varphi D_s \frac{\partial A}{\partial z}\right) - \frac{1}{\varphi}\frac{\partial}{\partial z}(\varphi v A) - \frac{K}{1-\varphi}\frac{\partial}{\partial z}(\omega(1-\varphi)A) + R_{prdn}\end{aligned}. \tag{A5}$$

Based on equations (7) and (8) in the text, the two "advective" terms here can be simplified as

$$(1+K)\frac{\partial A}{\partial t} = \frac{1}{\varphi}\frac{\partial}{\partial z}\left(\varphi D_s \frac{\partial A}{\partial z}\right) - \frac{W}{\varphi}\frac{\partial A}{\partial z} - \frac{KW(1-\varphi_\infty)}{(1-\varphi)\varphi_\infty}\frac{\partial A}{\partial z} + R_{prdn}, \tag{A6}$$

and this equation can be finally simplified to

$$\frac{\partial A}{\partial t} = \frac{1}{(1+K)}\frac{\partial}{\partial z}\left(\partial D_s \frac{\partial A}{\partial z}\right) - \frac{W}{\varphi}\left(\frac{1+\frac{K\varphi(1-\varphi_\infty)}{\varphi_\infty(1-\varphi)}}{1+K}\right)\frac{\partial A}{\partial z} + \frac{1}{(1+K)}R_{prdn}. \tag{A7}$$

Although equation (A7) appears rather complex, it is now in a form that can be incorporated into, and solved, in the OMSN model.

As a check on this solution, we note that when $K = 0$, the second (advective) term on the right side of equation (A7) simplifies to $\frac{W}{\varphi}\frac{\partial A}{\partial z}$ as in equation (7) in the main text. Finally, when $K \neq 0$, if we assume constant porosity and steady-state conditions, the second (advective) term on the right side of equation (A7) again simplifies to $\frac{W}{\varphi}\frac{\partial A}{\partial z}$, but here $\frac{W}{\varphi}$ simply equals ω, and the steady-state version of equation (A7) can be rewritten as

$$0 = \frac{D_s}{1+K}\frac{\partial^2 A}{\partial z^2} - \omega\frac{\partial A}{\partial z} + \frac{1}{1+K}R_{prdn}, \tag{A8}$$

which is the more commonly presented version of the RT equation including reversible adsorption (e.g., Berner 1976).

Finally, in using equation (A7) in the OMSN model (Section 4c) the equation for the kinetics of ammonium production is given by,

$$R_{prdn} = \sum_{i=1}^{3}\left[\frac{\Im k_i(1/r_{CNi})G_i S}{K_m + S} + f_S \Im k_i(1/r_{CNi})G_i\right], \tag{A9}$$

which represents ammonium regeneration associated with oSR and methanogenesis for each organic matter fraction, assuming that each fraction has a distinct carbon-to-nitrogen ratio, or r_{CNi}.

REFERENCES

Arndt, S., B. B. Jørgensen, D. E. LaRowe, J. J. Middelburg, R. D. Pancost, and P. Regnier. 2013. Quantifying the degradation of organic matter in marine sediments: A review and synthesis. Earth-Sci. Rev., *123*, 53–86. doi: 10.1016/j.earscirev.2013.02.008

Berelson, W. M., M. Prokopenko, F. J. Sansone, A. W. Graham, J. McManus, and J. M. Bernhard. 2005. Anaerobic diagenesis of silica and carbon in continental margin sediments: Discrete zones of TCO_2 production. Geochim. Cosmochim. Acta, *69*(19), 4611–4629. doi: 10.1016/j.gca.2005.05.011

Berner, R. A. 1976. Inclusion of adsorption in the modelling of early diagenesis. Earth Planet. Sci. Lett., *29*(2), 333–340. doi: 10.1016/0012-821X(76)90137-0

Bianchi, T. S. 2011. The role of terrestrially derived organic carbon in the coastal ocean: A changing paradigm and the priming effect. Proc. Nat. Acad. Sci., *108*, 19473–19481.

Bohrmann, G., and M. E. Torres. 2006. Gas hydrates in marine sediments, *in* Marine Geochemistry, H. D. Schultz and M. Zabel, editors. Berlin: Springer, 481–512.

Borowski, W. S., C. K. Paull, and W. Ussler III. 1997. Carbon cycling within the upper methanogenic zone of continental rise sediments: An example from the methane-rich sediments overlying the Blake Ridge gas hydrate deposits. Mar. Chem., *57*(3–4), 299–311. doi: 10.1016/S0304-4203(97)00019-4

Boudreau, B. P. 1997. Diagenetic Models and Their Implementation. Berlin: Springer-Verlag.

Boudreau, B. P., and B. R. Ruddick. 1991. On a reactive continuum representation of organic matter diagenesis. Am. J. Sci., *291*(5), 507–538.

Bruland, K. W., R. P. Franks, W. M. Landing, and A. Soutar. 1981. Southern California inner basin sediment trap calibration. Earth Planet. Sci. Lett., *53*(3), 400–408. doi: 10.1016/0012-821X(81)90044-3

Burdige, D. J. 1991. The kinetics of organic matter mineralization in anoxic marine sediments. J. Mar. Res., *49*(4), 727–761. doi: 10.1357/002224091784995710

Burdige, D. J. 2006. Geochemistry of Marine Sediments. Princeton, NJ: Princeton University Press.

Burdige, D. J. 2011. The temperature dependence of organic matter remineralization in deeply-buried marine sediments. Earth Planet. Sci. Lett., *311*(3–4), 396–410. doi: 10.1016/j.epsl.2011.09.043

Burdige, D. J., and T. Komada. 2011. Anaerobic oxidation of methane and the stoichiometry of remineralization processes in continental margin sediments. Limnol. Oceanogr., *56*(5), 1781–1796. doi: 10.4319/lo.2011.56.5.1781

Burdige, D. J., and T. Komada. 2013. Using ammonium pore water profiles to assess stoichiometry of deep remineralization processes in methanogenic continental margin sediments. Geochem., Geophys., Geosyst., *14*(5), 1626–1643. doi: 10.1002/ggge.20117

Canfield, D. E. 1994. Factors influencing organic matter preservation in marine sediments. Chem. Geol., *114*(3–4), 315–329. doi: 10.1016/0009-2541(94)90061-2

Chatterjee, S., G. R. Dickens, G. Bhatnagar, W. G. Chapman, B. Dugan, G. T. Snyder, and G. J. Hirasaki. 2011. Pore water sulfate, alkalinity, and carbon isotope profiles in shallow sediment above marine gas hydrate systems: A numerical modeling perspective. J. Geophys. Res.: Solid Earth, *116*, B09103. doi: 10.1029/2011JB008290

Christensen, C. J., D. S. Gorsline, D. E. Hammond, and S. P. Lund. 1994. Non-annual laminations and expansion of anoxic basin-floor conditions in Santa Monica Basin, California Borderland, over the past four centuries. Mar. Geol., *116*(3–4), 399–418. doi: 10.1016/0025-3227(94)90054-X

Dale, A. W., P. Regnier, N. J. Knab, B. B Jørgensen, and P. Van Cappellen. 2008. Anaerobic oxidation of methane (AOM) in marine sediments from the Skagerrak (Denmark): II. Reaction-transport modeling. Geochim. Cosmochim. Acta, *72*(12), 2880–2894. doi: 10.1016/j.gca.2007.11.039

Dickens, G. R. 2001. Sulfate profiles and barium fronts in sediment on the Blake Ridge: Present and past methane fluxes through a large gas hydrate reservoir. Geochim. Cosmochim. Acta, *65*(4), 529–543. doi: 10.1016/S0016-7037(00)00556-1

Emery, K. O. 1960. The Sea off Southern California. New York: John Wiley and Sons.

Harrison, B. K., H. Zhang, W. Berelson, and V. J. Orphan. 2009. Variations in archaeal and bacterial diversity associated with the sulfate-methane transition zone in continental margin sediments (Santa Barbara Basin, California). Appl. Environ. Microbiol., *75*(6), 1487–1499. doi: 10.1128/AEM.01812-08

Hedges, J. I., and R. G. Keil. 1995. Sedimentary organic matter preservation: An assessment and speculative synthesis. Mar. Chem., *49*(2–3), 81–115. doi: 10.1016/0304-4203(95)00008-F

Hein, J. R., W. R. Normark, B. R. McIntyre, T. D. Lorenson, and C. L. Powell II. 2006. Methanogenic calcite, ^{13}C-depleted bivalve shells, and gas hydrate from a mud volcano offshore southern California. Geology, *34*(2), 109–112. doi: 10.1130/G22098.1

Hill, T. M., J. P. Kennett, and H. J. Spero. 2004. High-resolution records of methane hydrate dissociation: ODP Site 893, Santa Barbara Basin. Earth Planet. Sci. Lett., *223*(1–2), 127–140. doi: 10.1016/j.epsl.2004.04.003

Hwang, J., E. R. M. Druffel, and T. Komada. 2005. Transport of organic carbon from the California coast to the slope region: A study of Δ^{14}C and δ^{13}C signatures of organic compound classes. Global Biogeochem. Cycles, *19*, GB2018. doi: 10.1029/2004GB002422

Inagaki, F., T. Nunoura, S. Nakagawa, A. Teske, M. Lever, A. Lauer, M. Suzuki, et al. 2006. Biogeographical distribution and diversity of microbes in methane hydrate-bearing deep marine sediments on the Pacific Ocean Margin. Proc. Natl. Acad. Sci. U. S. A., *103*(8), 2815–2820. doi: 10.1073/pnas.0511033103

Jahnke, R. A. 1990. Early diagenesis and recycling of biogenic debris at the seafloor, Santa Monica Basin, California. J. Mar. Res., *48*(2), 413–436. doi: 10.1357/002224090784988773

Jørgensen, B. B., and R. J. Parkes. 2010. Role of sulfate reduction and methane production by organic carbon degradation in eutrophic fjord sediments (Limfjorden, Denmark). Limnol. Oceanogr., *55*(3), 1338–1352. doi: 10.4319/lo.2010.55.3.1338

Komada, T., D. J. Burdige, S. M. Crispo, E. R. M. Druffel, S. Griffin, L. Johnson, and D. Le. 2013. Dissolved organic carbon dynamics in anaerobic sediments of the Santa Monica Basin. Geochim. Cosmochim. Acta, *110*, 253–273. doi: 10.1016/j.gca.2013.02.017

Komada, T., D. J. Burdige, H.-L. Li, C. Magen, J. P. Chanton, and A. K. Cada. 2016. Organic matter cycling across the sulfate-methane transition zone of the Santa Barbara Basin, California Borderland. Geochim. Cosmochim. Acta, *176*, 259–278. doi: 10.1016/j.gca.2015.12.022

Lapham, L. L., J. P. Chanton, R. Chapman, and C. S. Martens. 2010. Methane under-saturated fluids in deep-sea sediments: Implications for gas hydrate stability. Earth Planet. Sci. Lett., *298*(3–4), 275–285. doi: 10.1016/j.epsl.2010.07.016

Leifer, I., B. P. Luyendyk, J. Boles, and J. F. Clark. 2006. Natural marine seepage blowout: Contribution to atmospheric methane. Global Biogeochem. Cycles, *20*, GB3008. doi: 10.1029/2005GB002668

Lerman, A. 1977. Migrational processes and chemical reactions in interstitial waters, *in* The Sea, Vol. 6, Marine Modeling. E. D. Goldberg, I. N. McCave, J. J. O'Brien, and J. H. Steele, editors. New York: Wiley, 695–738.

Mackin, J. E., and R. C. Aller. 1984. Ammonium adsorption in marine sediments. Limnol. Oceanogr., *29*(2), 250–257. doi: 10.4319/lo.1984.29.2.0250

Martens, C. S., D. B. Albert, and M. J. Alperin. 1998. Biogeochemical processes controlling methane in gassy coastal sediments—Part 1. A model coupling organic matter flux to gas production, oxidation and transport. Cont. Shelf Res., *18*(14–15), 1741–1770. doi: 10.1016/S0278-4343(98)00056-9

MathWorks. 2016a. Create or Alter Options Structure for Ordinary Differential Equation Solvers: MATLAB odeset. http://www.mathworks.com/help/matlab/ref/odeset.html

MathWorks. 2016b. Solve Stiff Differential Equations and DAEs—variable Order Method: MATLAB ode15s. http://www.mathworks.com/help/matlab/ref/ode15s.html

Middelburg, J. J. 1989. A simple rate model for organic matter decomposition in marine sediments. Geochim. Cosmochim. Acta, *53*(7), 1577–1581. doi: 10.1016/0016-7037(89)90239-1

Mollenhauer, G., and T. I. Eglinton. 2007. Diagenetic and sedimentological controls on the composition of organic matter preserved in California Borderland Basin sediments. Limnol. Oceanogr., *52*(2), 558–576. doi: 10.4319/lo.2007.52.2.0558

Morse, J. W., D. K. Gledhill, and F. J. Millero. 2003. $CaCO_3$ precipitation kinetics in waters from the Great Bahama Bank: Implications for the relationship between bank hydrochemistry and whitings. Geochim. Cosmochim. Acta, *67*(15), 2819–2862. doi: 10.1016/S0016-7037(03)00103-0

Normark, W. R., D. J. W. Piper, and R. Sliter. 2006. Sea-level and tectonic control of middle to late Pleistocene turbidite systems in Santa Monica Basin, offshore California. Sedimentology, *53*(4), 867–897. doi: 10.1111/j.1365-3091.2006.00797.x

Parkes, R. J., G. Webster, B. A. Cragg, A. J. Weightman, C. J. Newberry, T. G. Ferdelman, J. Kallmeyer, B. B. Jørgensen, I. W. Aiello, and J. C. Fry. 2005. Deep sub-seafloor prokaryotes stimulated at interfaces over geological time. Nature, *436*, 390–394. doi: 10.1038/nature03796

Parkes, R. J., P. Wellsbury, I. D. Mather, S. J. Cobb, B. A. Cragg, E. R. C. Hornibrook, and B. Horsfield. 2007. Temperature activation of organic matter and minerals during burial has been the potential to sustain the deep biosphere over geological timescales. Org. Geochem., *38*(6), 845–852. doi: 10.1016/j.orggeochem.2006.12.011

Paull, C. K., W. R. Normark, W. Ussler III, D. W. Caress, and R. Keaten. 2008. Association among active seafloor deformation, mound formation, and gas hydrate growth and accumulation within the seafloor of the Santa Monica Basin, offshore California. Mar. Geol., *250*(3–4), 258–275. doi: 10.1016/j.margeo.2008.01.011

Pohlman, J. W., C. Ruppel, D. R. Hutchinson, R. Downer, and R. B. Coffin. 2008. Assessing sulfate reduction and methane cycling in a high salinity pore water system in the northern Gulf of Mexico. Mar. Pet. Geol., *25*(9), 942–951. doi: 10.1016/j.marpetgeo.2008.01.016

Prokopenko, M. G., D. E. Hammond, W. M. Berelson, J. M. Bernhard, L. Stott, and R. Douglas. 2006. Nitrogen cycling in the sediments of Santa Barbara Basin and Eastern Subtropical North Pacific: Nitrogen isotopes, diagenesis and possible chemosymbiosis between two lithotrophs (*Thioploca* and Anammox)—"riding on a glider." Earth Planet. Sci. Lett., *242*(1–2), 186–204. doi: 10.1016/j.epsl.2005.11.044

Reeburgh, W. S. 2007. Oceanic methane biogeochemistry. Chem. Rev., *107*(2), 486–513. doi: 10.1021/cr050362v

Reimers, C. E., C. B. Lange, M. Tabak, and J. M. Bernhard. 1990. Seasonal spillover and varve formation in the Santa Barbara Basin, California. Limnol. Oceanogr., *35*(7), 1577–1585. doi: 10.4319/lo.1990.35.7.1577

Reimers, C. E., K. C. Ruttenberg, D. E. Canfield, M. B. Christiansen, and J. B. Martin. 1996. Porewater pH and authigenic phases formed in the uppermost sediments of the Santa Barbara Basin. Geochim. Cosmochim. Acta, *60*(21), 4037–4057. doi: 10.1016/S0016-7037(96)00231-1

Schiesser, W. E. 1991. The Numerical Method of Lines: Integration of Partial Differential Equations. San Diego, CA: Academic Press.

Schimmelmann, A., C. B. Lange, and W. H. Berger. 1990. Climatically controlled marker layers in Santa Barbara Basin sediments and fine-scale core-to-core correlation. Limnol. Oceanogr., *35*(1), 165–173. doi: 10.4319/lo.1990.35.1.0165

Schulz, H. D., and M. Zabel. 2006. Marine Geochemistry, 2nd ed. Berlin: Springer-Verlag.

Shampine, L. F., and M. W. Reichelt. 1997. The MATLAB ODE suite. SIAM J. Sci. Comput., *18*(1), 1–22. doi: 10.1137/S1064827594276424

Sholkovitz, E. 1973. Interstitial water chemistry of the Santa Barbara Basin sediments. Geochim. Cosmochim. Acta, *37*(9), 2043–2073. doi: 10.1016/0016-7037(73)90008-2

Snyder, G. T., A. Hiruta, R. Matsumoto, G. R. Dickens, H. Tomaru, R. Takeuchi, J. Komatsubara, Y. Ishida, and H. Yu. 2007. Pore water profiles and authigenic mineralization in shallow marine sediments above the methane-charged system on Umitaka Spur, Japan Sea. Deep Sea Res., Part II, *54*(11–13), 1216–1239. doi: 10.1016/j.dsr2.2007.04.001

Soutar, A., and P. A. Crill. 1977. Sedimentation and climatic patterns in the Santa Barbara Basin during the 19th and 20th centuries. Geol. Soc. Am. Bull., *88*(8), 1161–1172. doi: 10.1130/0016-7606(1977)88<1161:SACPIT>2.0.CO;2

Thunell, R. C. 1998. Particle fluxes in a coastal upwelling zone: Sediment trap results from Santa Barbara Basin, California. Deep Sea Res., Part II, *45*(8–9), 1863–1884. doi: 10.1016/S0967-0645(98)80020-9

Wellsbury, P., K. Goodman, T. Barth, B. A. Cragg, S. P. Barnes, and R. J. Parkes. 1997. Deep marine biosphere fuelled by increasing organic matter availability during burial and heating. Nature, *388*, 573–576.

Westrich, J. T., and R. A. Berner. 1984. The role of sedimentary organic matter in bacterial sulfate reduction: The *G* model tested. Limnol. Oceanogr., *29*(2), 236–249. doi: 10.4319/lo.1984.29.2.0236

Zhu, Y., B. Shi, and C. Fang. 2000. The isotopic compositions of molecular nitrogen: Implications on their origins in natural gas accumulations. Chem. Geol., *164*(3–4), 321–330. doi: 10.1016/S0009-2541(99)00151-5

Received: *26 December 2015*; revised: *6 April 2016*.